Design and Application of an Asymmetric Naphthalimide-based Molecule with Improved Hydrophobicity for Highly Stable Organic Solar Cells

Qing Liao, Qian Kang, Bowei Xu,* and Jianhui Hou*

Read Online

ACCESS | Metrics & More | Article Recommendations | SI Supporting Information

ABSTRACT: With the photovoltaic efficiency of organic solar cells (OSCs) exceeding 17%, improving the stability of these systems has become the most important issue for their practical applications. In particular, moisture in the environment may erode the interlayer molecules, which has been proved to be the main reason for the efficiency decay. At present, the development of moisture-resistant interlayer molecules remains a great challenge to the field. Herein, we designed two naphthalene diimide (NDI)-based organic compounds, namely, NDI-M and NDI-S, exhibiting suitable energy level and excellent electron extraction property. In addition to this, NDI-S has extremely low hygroscopicity. An efficiency of 17.27% was achieved for the NDI-S inverted cells, and the long-term stability under continuous illumination conditions was significantly improved with a T80 lifetime (the time required to reach 80% of initial performance) of over 28 000 h. More importantly, we demonstrated that, by using a covalent bond to link the counter ions with the host molecular structure in the zwitterion, the asymmetric molecule NDI-S can transform from amorphous to crystalline hydrate at high humidity and exhibited outstanding non-hygroscopic nature; this could decrease the interaction between the cell and the moisture, obviously improving the device stability under high humidity.

KEYWORDS: non-fullerene organic solar cell, cathode interlayer, power conversion efficiency, stability, zwitterion, moisture-resistant
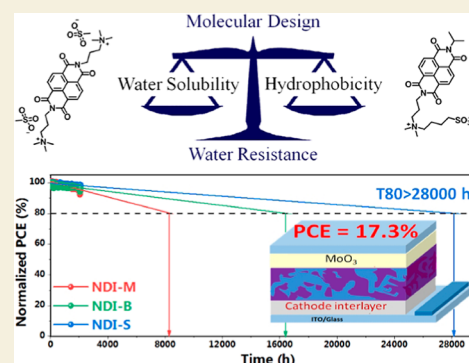
INTRODUCTION

The organic solar cell (OSC) has been considered as the next-generation photovoltaic technology with the advantage of fabricating large-area panel using the cost-effective solution processing method.[1−5] The power conversion efficiency (PCE) of the state-of-the-art OSC has exceeded 18%, reaching the threshold of practical use.[6−11] Compared to the advancement in PCE, the improvement in device stability is rather limited.[12−16] In particular, although OSCs with good storage stabilities in the dark or in an inert atmosphere have been reported, most devices exhibited dramatic performance decay in ambient conditions due to the fragility under external environmental factors.[17−24] In fact, it is an abnormal phenomenon that the pursuit of photovoltaic efficiency in the OSC field becomes the focus of attention, regardless of a long lifetime under the ambient conditions, and the neglect of a long lifetime makes no sense to an applied technology like organic photovoltaics.[25] At present, the poor ambient stability has become the main bottleneck for the practical application of OSCs. Thus, it is imperative to substantially improve the ambient stability of OSC devices.

Moisture can severely damage the stability of OSCs in the ambient air. Water molecules can permeate into the device, which not only traps free charges but also destroys the adhesion between the active layer and electrode, leading to the

decomposition of the device structure.[26−29] As a result, the OSC shows a significant PCE attenuation through a period of operation. Although the utilization of the encapsulation technology can effectively protect the OSC device from moisture ingress, the cell lifetime is highly dependent on the quality of encapsulation because a small leakage in the encapsulation package may result in a catastrophic collapse of the device performance.[30−32] Even with careful encapsulation, both the corrosion effect of ambient conditions and the long-term permeation of moisture can inevitably lead to the degradation of OSC performances.[33,34] Recent research results indicated that the electrode interlayer plays a key role in the stability of OSCs. For instance, Hou et al. designed and synthesized a naphthalene diimide (NDI)-based small-molecule NDI-B as a cathode interlayer, which can protect the active layer from ultraviolet damage, so that a lifetime of over 2000 h under 1-sun illumination conditions was
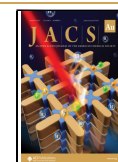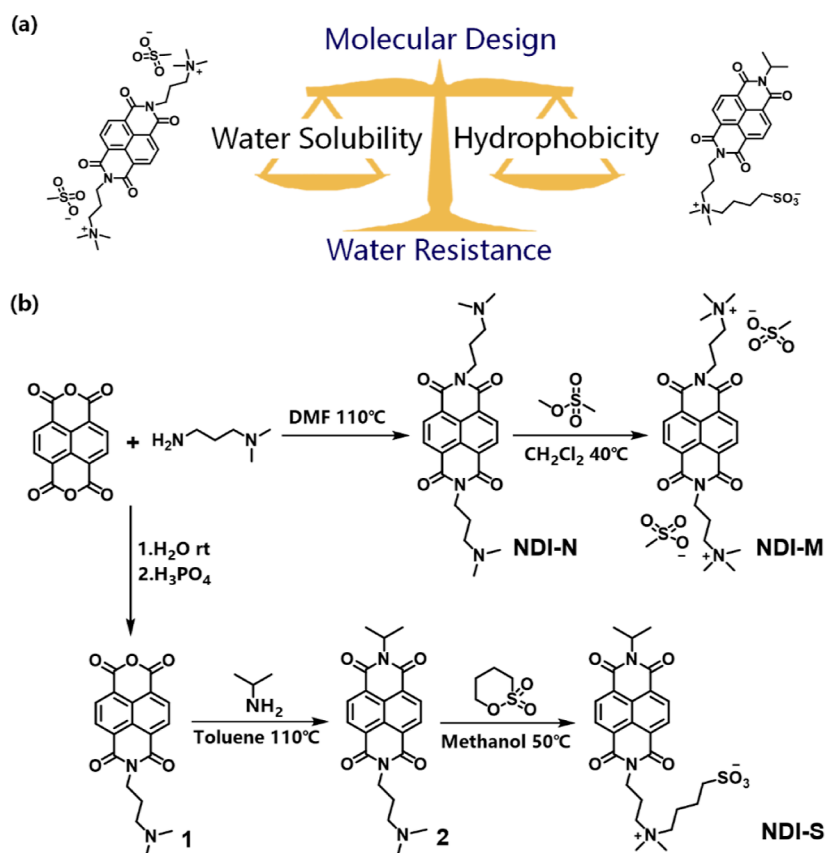
Figure 1. (a) Molecular design to balance water solubility and hygroscopicity. (b) Synthetic route of NDI-M and NDI-S.

achieved.[35] Moreover, Shao et al. developed a MoO$_3$-PEDOT:PSS composite film as the anode interlayer that can effectively prevent the diffusion of oxygen into OSCs and improved the ambient stability of the device.[36] However, suffering from the hygroscopic nature, most electrode interlayers are susceptible to moisture, which impedes the further improvement of device stability. So far, no effective method has been reported to solve the problem of water ingress in OSCs. Thus, it is of considerable significance to develop new interlayer molecules with non-hygroscopic property and realize high device stability under ambient conditions.

Herein, by the rational design, we synthesized an asymmetric naphthalimide (NDI)-based molecule NDI-S with balanced characteristics between solubility and hydrophobicity (Figure 1a), which could effectively improve the OSC stability by inhibiting moisture ingression. A symmetric molecule NDI-M with high water solubility was also synthesized for comparison. Both NDI-M and NDI-S possess exceptional optical transparency, suitable energy level, and excellent electron extraction property, making them ideal candidates in serving as interlayers for cathode modification. OSCs using NDI-M, NDI-S, and the reported NDI-B as CILs exhibited similar PCE values of about 17.3%, which represents the highest level of photovoltaic efficiency in the OSC field. Besides high PCE, the encapsulated devices with NDI-M, NDI-S, and NDI-B all showed excellent operational stability under 1-sun illumination due to the ultraviolet resistance of the NDI-based CIL. Most importantly, we demonstrated that, by using a covalent bond to link the counter ions with the host molecular structure in the zwitterion, the asymmetric molecule NDI-S can transform

from amorphous to crystalline hydrate at high humidity and exhibited outstanding non-hygroscopic nature; this could decrease the interaction between the cell and the moisture, obviously improving the device stability under high humidity. The results of dynamic vapor sorption (DVS) measurements indicated that NDI-M, NDI-S, and NDI-B had equilibrium moisture contents of 85, 10, and 15% at a relative humidity (RH) of 95%, respectively, implying that NDI-S has the best moisture resistance. For device fabrication, the ionized end group in NDI-M can induce a deliquescence process of the CIL and the mobile counter ions may diffuse across the device. As a result, OSCs with NDI-M showed a fast attenuation of PCE under the humidity condition. Using NDI-S as the CIL, the OSC device without any encapsulation can maintain 93% of its initial PCE after a storage period of 168 h under the RH of 80% and the temperature of 25 °C. To the best of our knowledge, at present, it is the best result of OSC device to resist humidity, implying that an exceptional ambient stability can be achieved by using NDI-S as the CIL.

■ EXPERIMENTAL SECTION

Synthesis Details

(N,N-Dimethylamino) Propyl Naphthalene Diimide (NDI-N). 1,4,5,8-Naphthalenetetracarboxylic dianhydride (4.36 g, 10 mmol) was added to a 250 mL two-necked flask. After being flushed by a gentle stream of dry argon, 100 mL of dimethylformamide (DMF) and N,N-dimethyl-1,3-propane diamine (3 mL, 21 mmol) were added successively. To this suspension, triethylamine (1 mL) was added and allowed to reflux for 12 h. After cooling the reaction mixture to ambient temperature, the precipitate was filtered and recrystallized from ethanol. A light yellow solid crystal was obtained with a yield of

75%. ^{1}H NMR (400 MHz, CDCl$_3$, δ): 8.75 (s, 4H), 4.27 (t, 4H), 2.49 (t, 4H), 2.28 (s, 12H), 1.96 (m, 4H) (Figure S17).

3,3′-(1,3,6,8-Tetraoxo-1,3,6,8-tetrahydrobenzo[*lmn*][3,8]-phenanthroline-2,7-diyl)bis(*N*,*N*,*N*-trimethylpropan-1-aminium) Methanesulfonate (NDI-M). To a 250 mL two-necked flask, (*N*,*N*-dimethylamino) propyl naphthalene diimide (1.31 g, 3 mmol) was added. After being flushed by a gentle stream of dry argon, trichloromethane (60 mL) was injected into the flask, and then, methyl methanesulfonate (1.12 g, 10.2 mmol) was added dropwise into this mixture. The mixture was further stirred for 48 h at 58 °C, and the formed precipitate was filtered off and washed with dichloromethane and ethyl acetate. The crude product was recrystallized from a mixture of water and methanol to obtain a colorless crystalline solid (1.58 g, yield 80%).^{1}H NMR (400 MHz, D$_2$O, δ): 8.63 (s, 4H), 4.27 (t, 4H), 3.56 (t, 4H), 3.18 (s, 18H), 2.80 (s, 6H), 2.31 (m, 4H) (Figure S18). ESI-MS: *m/z* calcd for $[C_{26}H_{34}N_4O_4]^{2+}[CH_3O_2S]^{2-}$, 466, 95; found: 233, 95 (Figure S22). Anal. calcd for $[C_{26}H_{34}N_4O_4]^{2+}[CH_3O_2S]^{2-}$: C 51.21, H 6.14, N 8.53, O 24.36, S 9.76; found: C 49.43, H 6.30, N 8.22, O 26.65, S 9.40.

7-(3-(Dimethylamino)propyl)-1*H*-isochromeno[6,5,4-*def*]-isoquinoline-1,3,6,8(7*H*)-tetraone (1). 1,4,5,8-naphthalenetetra-carboxylic acid dianhydride (10.00 g, 37.3 mmol) was taken in water (175 mL), followed by the addition of 1 M aqueous KOH solution (35 mL). This mixture was vigorously stirred and heated until almost the compound was dissolved. The pH of the resultant solution was acidified to 6.4 by adding 1 M H$_3$PO$_4$. To this solution, *N*,*N*-dimethyl-1,3-propane diamine (5.35 mL, 37.3 mmol) was added and the pH of the solution was readjusted to 6.4 with 1 M H$_3$PO$_4$. The mixture was heated to reflux overnight. It was then allowed to cool to room temperature and filtered. To the filtrate, acetic acid (125 mL) was added, a solid precipitate was formed, which was then filtrated and dried under vacuum to afford 9.45 g of pale yellow solid. This product was used without further purification in the next step.

2-(3-(Dimethylamino)propyl)-7-isopropylbenzo[*lmn*][3,8]-phenanthroline-1,3,6,8(2*H*,7*H*)-tetraone (2). 1 (2.96 g, 8.4 mmol) was added to a 250 mL two-necked flask. After being flushed by a gentle stream of dry argon, 120 mL of DMF and isopropylamine (1.64 g, 27.7 mmol) were added successively. Then, this suspension was allowed to reflux for 24 h. After cooling the reaction mixture to ambient temperature, the mixture was pulled into 250 g of ice and a yellow solid was precipitated. The precipitate was filtered and purified by column chromatography (silica gel, dichloromethane/triethyl-amine = 125:1) to obtain the corresponding product as a pale yellow crystal (2.15 g, 65% yield). ^{1}H NMR (400 MHz, CDCl$_3$, δ): 8.73 (s, 4H), 5.43 (m, 1H), 4.27 (t, 2H), 2.51 (t, 2H), 2.29 (s, 6H), 1.97 (m, 2H), 1.62 (d, 6H) (Figure S19).

4-((3-(7-Isopropyl-1,3,6,8-tetraoxo-3,6,7,8-tetrahydro-benzo[*lmn*][3,8]phenanthrolin-2(1H)-yl)propyl)dimethyl-ammonio)butane-1-sulfonate (NDI-S). To a 250 mL two-necked flask, compound **2** (1.18 g, 3 mmol) was added. After being flushed by a gentle stream of dry argon, methanol (120 mL) was injected into the flask, and then, 1,4-butane sultone (1.23 g, 9 mmol) was added into this mixture. The mixture was further stirred for 48 h at 65 °C. After cooling the reaction mixture to ambient temperature, the solution was concentrated by a rotary evaporator and then added dropwise to 500 mL of acetone. The formed precipitate was filtered off and washed with dichloromethane and ethyl ether. The crude product was recrystallized from a mixture of water and methanol to obtain a white crystalline solid (1.30 g, yield 82%).^{1}H NMR (400 MHz, D$_2$O, δ): 8.46 (s, 4H), 5.32 (m, 1H), 4.22 (t, 2H), 3.58 (t, 2H), 3.47 (t, 2H), 3.03 (s, 6H), 3.01 (t, 2H), 2.31 (m, 2H), 2.02 (m, 2H), 1.99 (m, 2H), 1.65 (d, 6H) (Figure S20). ESI-MS: *m/z* calcd for C$_{26}$H$_{31}$N$_3$O$_7$S, 529; found, 552 (Figure S21). Anal. calcd for C$_{26}$H$_{31}$N$_3$O$_7$S: C 58.97, H 5.90, N 7.93, O 21.15, S 6.05; found: C 57.14, H 5.69, N 7.52, O 23.73, S 5.92.

Fabrication and Characterization of OSC Devices

The structure of the solar cell on the glass substrate was indium tin oxide (ITO)/cathode interlayer/active layers/MoO$_3$/Al. Pre-patterned ITO-coated glass with a sheet resistance of 10−15 Ω/square was cleaned by sequential sonication in deionized water, acetone, and ethyl alcohol twice for 15 min. The pre-cleaned ITO-coated glass substrates were UV/ozone-treated for 20 min. For ZnO CIL preparation, the 2-methoxyethanol solution of zinc acetate dihydrate with a concentration of 100 mg mL^{-1} was made first, and a little amount of triethylamine was needed to enhance the solubility of zinc acetate dihydrate. Then, the precursor solution was spin-coated onto the ITO substrate at 3000 rpm for 30 s. The substrates were annealed for 1 h at 200 °C. For NDI-M, NDI-S, and NDI-B CIL preparation, the aqueous solution of the corresponding CIL with a concentration of 3.5 mg mL^{-1} was spin-coated onto the ITO substrate at 3000 rpm for 30 s without annealing. Then, all CIL coated substrates were transferred to the nitrogen-filled glovebox. The active layer materials were dissolved in chloroform with a concentration of 7.5 mg mL^{-1} containing the donor/acceptor (1/1.2 weight ratio). The solution needed to be heated at 45 °C until total dissolution. The active layers were spin-coated onto the cathode interlayer-modified substrate at 3500 rpm for 30 s after addition of 0.5% (volume ratio) of 1,8-diiodooctane. After that, the blend films were annealed under 100 °C for 10 min. Finally, 10 nm MoO$_3$ and 100 nm Al anode were evaporated sequentially under vacuum at 2×10^{-4} Pa. The device area was 0.04 cm^2.

The current density−voltage (*J*−*V*) characteristics were recorded with an Agilent B2912A Precision Source/Measure unit. The *J*−*V* curve was tested using the solar simulator (SS-F5-3A, Enlitech) along with AM 1.5G spectra, whose intensity was calibrated by the certified standard silicon solar cell (SRC-2020, Enlitech) at 100 mW cm^{-2}. The effective area of the device is 0.04 cm^2. External quantum efficiency (EQE) was measured using the solar-cell spectral-response measurement system QE-R3011 (Enli Technology Co., Ltd).

CIL thickness was obtained through a surface profilometer (Dektak XT, Bruker). The CIL film thickness in less than 10 nm was determined by calibration curves. First, we accurately measured the thicknesses of several thick films over 10 nm by both the step profiler and the UV−vis absorption intensities of the corresponding films. Then, a linear relationship of absorption intensity with thickness was established. Lastly, the film thickness in less than 10 nm was obtained through the calibration curve from measuring the absorption intensity of the ultrathin film (Figure S5).

Electrochemical Impedance Spectroscopy

The electrochemical impedance spectroscopy (EIS) measurement was performed using a E4990A Impedance Analyzer with a 20 mV ac signal at frequencies from 5 MHz to 20 Hz under the illumination of AM 1.5G, 100 mW cm^{-2}. A bias voltage equal to *Voc* was applied to offset the total current.

Photostability Measurement of OSC Devices

Devices were sealed by glass and tested in air. An array of white light-emitting diodes was used as the light source with an intensity equivalent to 1 Sun, which was calibrated by matching the device performance to those measured under AM 1.5 G. The initial exposure time is defined as time 0 s. The devices were kept under open-circuit conditions. The temperature of the cells was 45−55 °C during measurements.

DVS Measurement

Water sorption isotherms were recorded by a DVS analyzer (Vsorp Enhanced, ProUmid, Germany) at 25 °C. Stoichiometric ratio (RS) can be calculated by the equation

$$RS = \text{Moisture uptake} \times \frac{Mw_{sample}}{Mw_{water}} \qquad (1)$$

■ RESULTS AND DISCUSSION

The chemical structures and synthetic routes of NDI-M and NDI-S are shown in Figure 1b. NDI-N was prepared according to the literature method. The product NDI-M ammonium alkanesulfonate salt was synthesized by the alkylation reaction of NDI-N with methyl methanesulfonate. The NDI-based
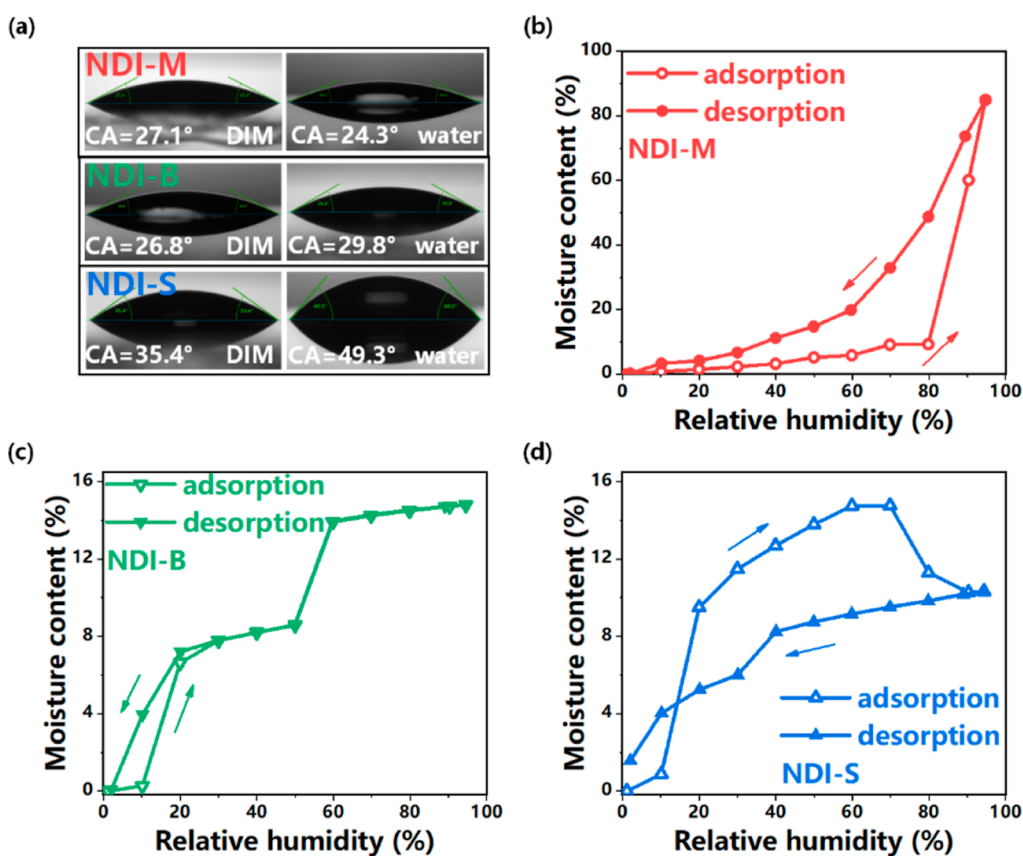
Figure 2. (a) Contact angles of diiodo-methane (DIM) and water dropped on the CIL surface. DVS moisture adsorption (empty points) and desorption (solid points) profiles of (b) NDI-M, (c) NDI-B, and (d) NDI-S samples. The raw data of DVS are presented in Figure S2.

precursor of NDI-S was synthesized by a simple two-step reaction using commercially available compounds, 1,4,5,8-naphthalenetetracarboxylic dianhydride, *N,N*-dimethyl-1,3-propane-diamine, and dimethylamine, as starting materials. The final product NDI-S zwitterion was synthesized by amine-induced ring−opening reactions of 1,4-butane sultone with the NDI-based precursor, giving good yields over 80%. Furthermore, the molecular structures of NDI-M and NDI-S have been characterized by ^{1}H nuclear magnetic resonance, EI mass spectrometry (Figures S17−S22), and elemental analysis. Both NDI-M and NDI-S can be dissolved in water and are completely insoluble in organic solvents such as chloroform, toluene, and chlorobenzene, which are widely used in making the active layers in OSCs; this factor is crucial for the multilayer deposition in OSC fabrication.

In order to achieve solvent orthogonality for multilayer depositions, the introduction of polar groups is usually required in the design of CIL molecules. However, the hygroscopicity of polar groups makes CIL molecules vulnerable to moisture erosion. As a result, the stability of devices based on these CIL molecules becomes susceptible to environmental humidity. To study the effect of polar groups on hygroscopicity, we investigated the hygroscopicity of NDI-M, NDI-B (NDI-B in Figure S1), and NDI-S molecules. Although these NDI-based molecules are all zwitterions, NDI-S and NDI-B have one and two alkyl sulfonate groups pendant from the quaternary ammonium salt group, respectively. However, the two alkyl sulfonate groups of NDI-M are not bonded to the limb structure of NDI-M. Differences in polar groups in these CILs may lead to differences in the surface energy and

hygroscopicity of these CILs, further affecting the stability of devices using these CILs in moisture. As shown in Figure 2a, the NDI-S film shows a higher water and diiodo-methane CA (contact angle), implying a more hydrophobic surface than the NDI-M or NDI-B film. The surface energies (γ_S) calculated by the Wu model are 59.38 mN/m for NDI-S, 73.88 mN/m for NDI-M, and 72.33 mN/m for NDI-B. Compared to the NDI-M or NDI-B film, the distinct hydrophobicity of the NDI-S film is not only beneficial for improving the wettability of the nonpolar solvent used to prepare the photoactive layer upon NDI-S but is also favorable to enhance the endurance to moisture for devices based on NDI-S.[37] Moisture sorption/desorption studies were performed by using the DVS method to investigate the hydration and dehydration behavior of these CILs. For each investigated CIL molecule, the moisture sorption/desorption isotherms reported in Figure 1b−d show the evolution of moisture content versus ambient air RH at a constant temperature of 25 °C. As shown in Figure 2b, the moisture uptake of NDI-M is about 10 wt % when the RH is less than 80%. Also, the moisture uptake of NDI-M increases dramatically when the RH is greater than 80%, indicating that NDI-M begins to deliquesce.[38,39] As the RH increases to 95%, the moisture uptake of NDI-M increases up to 85 wt %. The strong hygroscopicity of NDI-M reveals the intrinsic instability of the non-bonded zwitterion in high humidity environments. In Figure 2c, the moisture uptake of NDI-B is 15 wt % at 95% RH, and its adsorption and desorption isotherms are basically the same. We can observe that the moisture absorption of NDI-B is relatively stable in the RH ranges of 95−60% and 50−20%, and the average moisture adsorption for these two
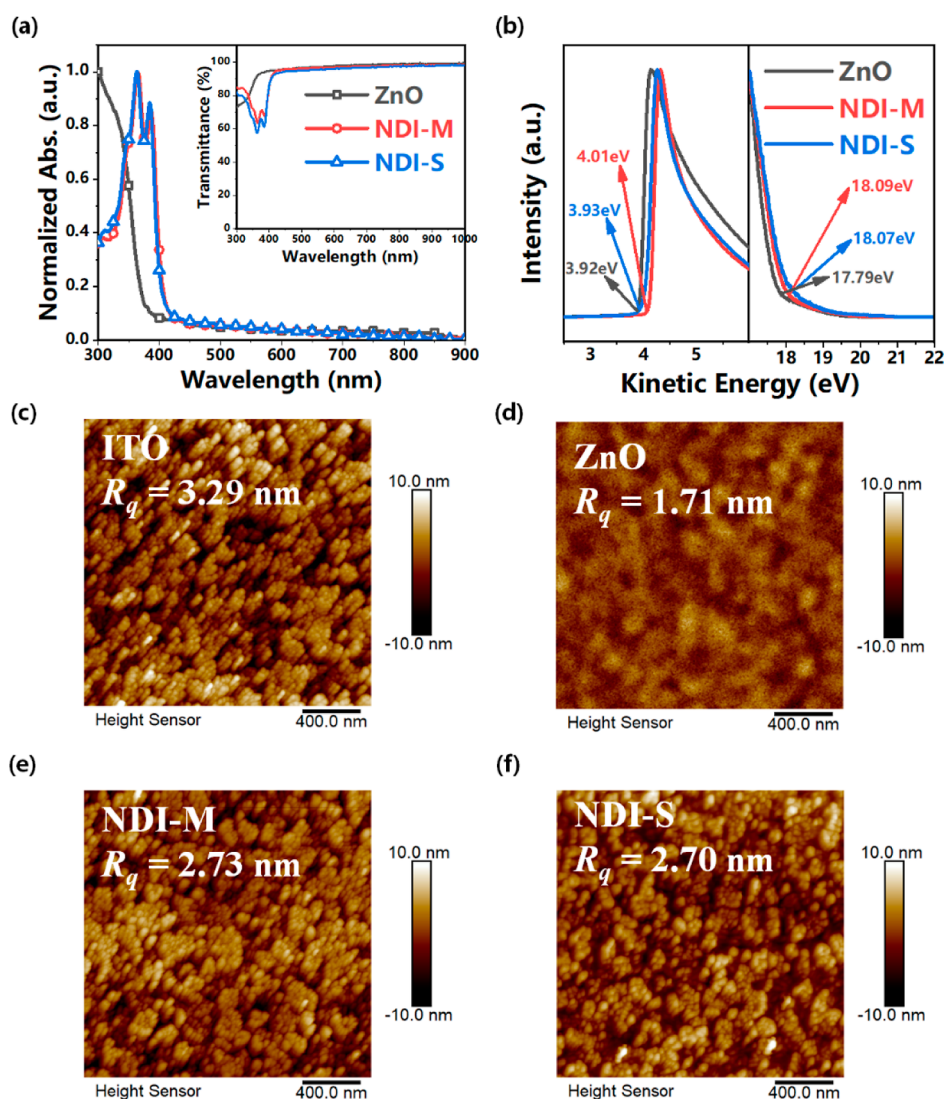
Figure 3. (a) Normalized ultraviolet−visible absorption spectra of ZnO, NDI-M, and NDI-S as films. The inset shows their transmittance spectra. (b) UPS of ZnO, NDI-M, and NDI-S films. AFM topography images of (c) ITO, (d) ZnO, (e) NDI-M, and (f) NDI-S films. All UPS and AFM characterizations were taken from the samples on ITO substrates.

ranges are 14.59 and 7.95 wt %, respectively. According to equation (1) in the experimental section, the RS between water and NDI-B was calculated to be 5.73 for the RH range of 95−60% and 3.12 for the RH range of 50−20%, which corresponds to the formation of the hexahydrate and trihydrate.[40,41] The hygroscopicity of NDI-B is much lower than that of NDI-M, and the hydrates formed in the above RH ranges are stable, which makes the stability of devices using NDI-B significantly higher than that of NDI-M. As for NDI-S, it can be seen in Figure 2d that there was a continuous increase in mass, which was attributed to the sorption of moisture in the RH range from 0 to 60%. At 70% RH, the mass suddenly decreased, which was ascribed to crystallization. With the lattice rearrangement during crystallization, vapor is expelled from the crystal lattice.[42,43] In order to prove that there was a change from the amorphous to the crystalline state in NDI-S, powdered X-ray diffraction experiments before and after the moisture sorption were performed. Figure S3 shows that the diffraction peaks appeared after moisture sorption, verifying the transition from amorphous to crystalline in NDI-S. After the RH was further increased, the final moisture uptake at 95%

RH was measured as 10 wt % for the crystalline NDI-S. During the desorption process, the moisture uptake of NDI-S was stable in the RH range from 95 to 60%, and the corresponding RS was calculated to be 2.88, indicating the formation of crystalline trihydrate. The extremely low hygroscopicity of amorphous NDI-S ensures the stability of devices using NDI-S as the CIL under a humid atmosphere, and the transformation of NDI-S from amorphous to crystalline trihydrate under a high RH environment can reduce the amount of moisture absorption, which may further improve the stability of the device, making it promising for practical use.

Figure 3a shows the absorption spectra of NDI-M and NDI-S as solid films, and the inset shows their transmittance spectra. The absorption band in the 300−400 nm range is typical for the NDI core, and the polar ammonium alkanesulfonate group does not change the optical properties of the NDI core. Moreover, both the NDI-M and NDI-S films show a good transparency between 450 and 1000 nm, which indicates that these CILs have small optical losses, being beneficial for achieving larger short-circuit current (J_{SC}). The conductivities of the NDI-M and NDI-S films were measured by using the
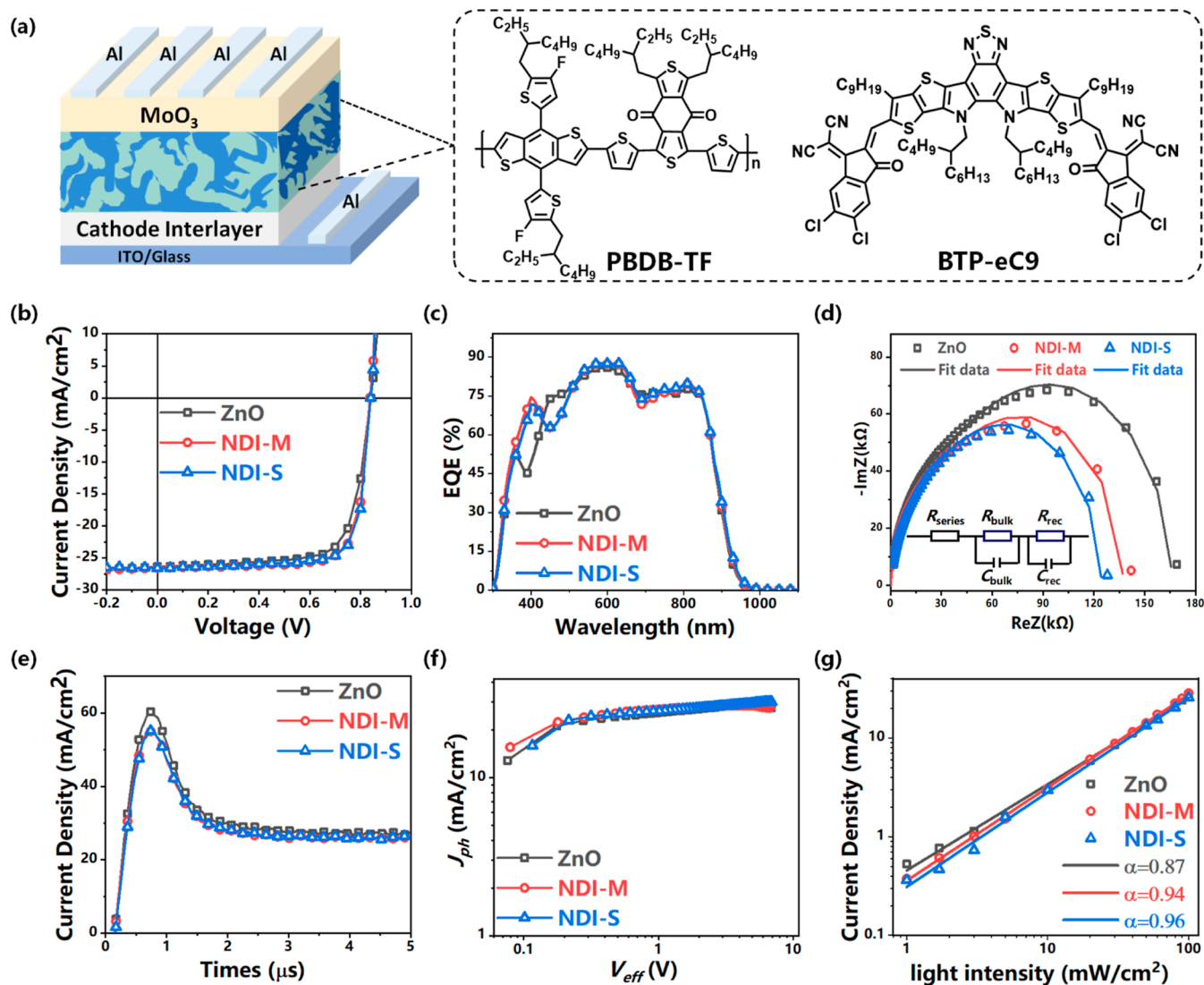
Figure 4. (a) Device structure of the OSCs used in this work and chemical structures of active layers. (b) $J-V$ characteristics of OSCs with ZnO, NDI-M, and NDI-S. (c) EQE characteristics of OSC devices with ZnO, NDI-M, and NDI-S as CILs. (d) Nyquist plot of impedance spectra measured on OSCs with different CILs. Inset: the equivalent-circuit model employed for fitting of EIS data. (e) Photo-CELIV curves of the devices. (f) Photocurrent (J_{ph}) versus effective voltage (V_{eff}) curves. (g) Jsc of the devices as a function of light intensity.

Table 1. Optimized Photovoltaic Parameters of Devices Based on ZnO, NDI-M, and NDI-S under the Illumination of AM 1.5G, 100 mW cm^{-2}

CILs	V_{oc} [V]	J_{sc} [mA cm^{-2}]	FF	PCE[a] [%]	J_{sc}^{cal} [mA cm^{-2}]	R_s [Ω cm^2]	R_{sh} [kΩ cm^2]
ZnO	0.84	26.37	73.57	16.20 (15.68 ± 0.30)	25.48	3.16	757.58
NDI-M	0.84	26.58	77.53	17.25 (17.01 ± 0.27)	25.66	2.27	746.27
NDI-S	0.84	26.61	77.26	17.27 (17.08 ± 0.23)	25.82	2.30	1706.23

[a]Data in brackets are average PCE values obtained from at least eight individual devices.

two-point probe method. The devices with a structure of ITO/CIL/Al were fabricated, and the *I-V* characteristics were tested. As shown in Figure S4, the conductivities of the ZnO, NDI-M, and NDI-S films are calculated to be 4.75×10^{-4}, 5.08×10^{-4}, and 6.65×10^{-4} S/m, respectively. The high conductivity of NDI-M and NDI-S can facilitate charge transport and effectively depress the charge recombination at the active layer/cathode interface. The work function (WF) is a key factor to determine the CIL performance of NDI-M and NDI-S. By using the secondary electron cut-off in the high binding energy (kinetic energy) region of the UPS spectrum, we can

obtain the WF of ZnO, NDI-M, and NDI-S to be 3.92, 3.93, and 4.01 eV (Figure 3b), respectively. Compared with the WF value of ITO (4.71 eV), these CILs drastically reduce the WF of ITO, so as to provide the better energy level alignment with the photoactive layers, facilitating the charge injection into the electrodes.[44] The reduction of WF in NDI-M and NDI-S also ensures that they can be perfectly used in inverted OSCs. Since the good film formation is a fundamental requirement for CILs, surface morphology of the CILs on the ITO substrate was investigated by atomic force microscopy (AFM). As shown in Figure 3c−f, the bare ITO substrate showed a root-mean-

square roughness (R_q) of 3.29 nm, while after modifying with ZnO, NDI-M, and NDI-S, the R_q values of the ITO substrates were decreased to 1.71, 2.73, and 2.70 nm, respectively. The smooth surfaces of NDI-M and NDI-S CILs are favorable to form good physical and electronic contact between CIL and ITO.

Based on the advantages mentioned above, we prepared inverted OSC devices with NDI-M and NDI-S to investigate their performances as CILs. Since ZnO is the most widely used CIL material in inverted devices, the device modified with ZnO was also fabricated as a comparison. The device structure and the photovoltaic materials (PBDB-TF and BTP-eC9) for the active layer are shown in Figure 4a. $J-V$ characteristics of the optimal OSCs with the as-studied CILs are displayed in Figure 4b, and the relevant photovoltaic parameters are listed in Table 1. Figure 4c shows EQE curves, and the integrated currents from the EQE spectra are in good agreement with the Jsc values measured from the $J-V$ curves. The optimal thickness was found to be 10 nm for both NDI-M and NDI-S, which is determined by calibration curves (Figure S5). Under AM 1.5 G, 100 mW cm^{-2} illumination, the device with NDI-S achieves a good PCE of 17.27%, along with a Voc of 0.84 V, a Jsc of 26.61 mA cm^{-2}, and an FF of 77.26%, representing the state-of-the-art photovoltaic performance of inverted OSCs. The NDI-M-modified OSC showed a PCE of 17.25%, which is similar to that of the NDI-S device. Both NDI-S and NDI-M devices exhibit higher PCE than that of ZnO devices (PCE = 16.30%). As reported in many studies, the high conductivity is favorable to developing thickness-insensitive interlayer materials. Thus, we investigate the effect of CIL thickness on device performance. As shown in Figure S6, both NDI-M and NDI-S exhibit outstanding tolerance to thickness variation in fabricating OSCs, that is, the OSCs with 100-nm NDI-M and NDI-S exhibited high PCEs of 14.19% and 14.66%, respectively. The results suggest that NDI-M and NDI-S are thickness-insensitive CIL materials, making them promising to be used in large-area fabrication.

Besides ZnO, other representative CIL materials such as PFN-Br and PNDIT-F3N-Br were also used as CILs for fabricating OSC devices. As shown in Figure S7, the control OSC devices based on PFN-Br and PNDIT-F3N-Br exhibited PCEs of 15.69 and 15.53%, respectively. The photovoltaic performances of the OSCs with PFN-Br and PNDIT-F3N-Br are inferior to the NDI-S or NDI-M devices. In particular, compared to the control devices, the OSCs based on NDI-S and NDI-M showed much higher FF values, suggesting the superior electron collection ability of the NDI-based CILs. Moreover, the J_{SC} of OSCs could also be greatly improved by using the NDI-M and NDI-S CILs, which should be ascribed to the photoelectric conversion ability of NDI-M and NDI-S. The remarkable improvement in PCE of the NDI-S- and NDI-M-based devices stems from the substantial increase in the key device parameters of Jsc (from 26.37 to 26.61 mA cm^{-2} and 26.58 mA cm^{-2}) and FF (from 73.57 to 77.26% and 77.53%) in comparison with the ZnO-based device. The improvement of Jsc and FF is mainly related to the interfacial contact and electron extraction. The energy level diagram of each component in the inverted devices is shown in Figure S8. The WF of ITO covered with NDI-S and NDI-M is located above the LUMO level of the electron acceptor BTP-eC9, which is the same as ZnO. According to the integer charge-transfer model, such energy level alignments can cause spontaneous charge transfer from the acceptor to the CILs,

which is essential for the formation of barrier-free interfacial contact.[45] In order to investigate the interfacial resistance which is closely related to the interfacial contact, the EIS measurement was performed by using a E4990A Impedance Analyzer with a 20 mV ac signal at frequencies from 5 MHz to 20 Hz under the illumination of AM 1.5G, 100 mW cm^{-2}. A bias voltage equal to V_{OC} was applied to offset the total current. Fitting by Nyquist and an equivalent-circuit model is shown in the inset of Figure 4d,[46,47] and the series resistance (R_{series}) values were determined to be 351, 372, and 780 Ω for the devices with NDI-S, NDI-M, and ZnO, respectively. The lower R_{series} values means fewer interfacial defects for the devices modified with NDI-S and NDI-M, which may further depress the charge recombination. The decreasing interfacial defects can reduce current leakage of the device by reducing trapping of the film. Figure S9 displays the dark $J-V$ curves of devices modified with these CILs. Obviously, the dark current of NDI-S- and NDI-M-treated devices indicated more restrained leakage current under reverse bias voltage and higher current under forward bias and produced a rectification ratio larger than that of the ZnO device, proving that carrier injection registered was improved after NDI-S and NDI-M modification.[48] All these results proved that better interfacial contact was formed in NDI-S and NDI-M devices.

The superior electron extraction capacity of NDI-S and NDI-M to ZnO was investigated by the measurements of carrier mobility, exciton dissociation, and carrier recombination. The carrier mobilities of the OSCs with NDI-S, NDI-M, and ZnO were characterized by using the linearly increasing voltage (photo-CELIV) measurement to be 2.05×10^{-4}, 2.03×10^{-4}, and 1.31×10^{-4} cm$^2 \cdot$V$^{-1} \cdot$s^{-1}, respectively, as shown in Figure 4e. The high charge mobility demonstrates the excellent electron extraction and transport properties of the device with NDI-S and NDI-M. The built-in voltage (V_{bi}) of devices was estimated by means of Mott−Schottky analysis. Based on the fitting data in Figure S10 (dashed lines), the V_{bi} of ZnO is 0.56 V, which is much lower than that of NDI-S (0.60 V) and NDI-M (0.60 V). The larger V_{bi} of NDI-S and NDI-M suggests that the ideal internal electric field can be achieved in the devices, and thus, the exciton dissociation may be improved. To further demonstrate the above-mentioned points, we measured the photocurrent density (J_{ph}) versus the effective voltage ($V_{eff} = V_{bi} - V_{app}$, where V_{app} is the applied bias) of OSCs with these CILs.[49] As shown in Figure 4f, the exciton dissociation probabilities (P_{diss}) of the devices were 97.8% for NDI-S, 96.9% for NDI-M, and 93.9% for ZnO. The lower P_{diss} value of the ZnO device than that of NDI-S and NDI-M devices indicated that the relative devices were affected more by efficiently dissociated excitons, and so, the ZnO device can only generate poorer J_{SC} and FF. Similarly, it is observed that NDI-S and NDI-B could better suppress the carrier recombination. The charge recombination behavior of the OSCs was evaluated by the dependence of J_{SC} on the light intensity (P), as well as the dependence of Voc on P.[50] In Figure 4g, according to the law of $J_{SC} \propto P$,[51] the fitted slopes for NDI-S and NDI-M devices are 0.96 and 0.94, respectively, approaching closely to 1, while the slope of ZnO device is 0.87. This means that there is effective carrier collection and well-suppressed bimolecular recombination in the OSCs with NDI-S and NDI-M as CILs. The slope of V_{OC} versus $\ln(P)$ line should be kT/q for bimolecular recombination,[50] while the competition between bimolecular and Shockley−Read−Hall type, trap-assisted recombination makes the slope between $kT/$
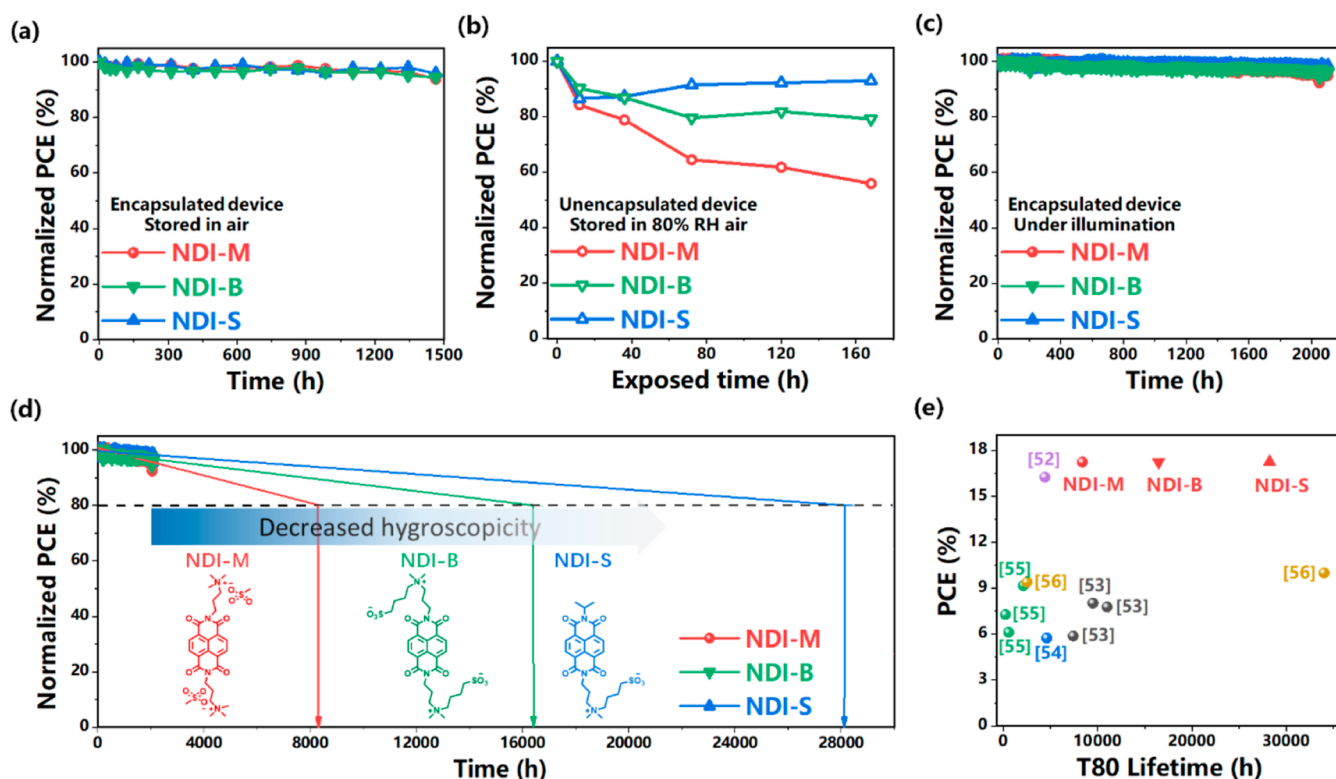
Figure 5. (a) Storage stability of the encapsulated devices with NDI-M, NDI-S, and NDI-B CILs in air. (b) Normalized PCE values as a function of exposure time in an 80% RH environment at 25 °C for devices modified with NDI-M, NDI-S, and NDI-B. (c) Photo-stability of the NDI-M, NDI-S, and NDI-B devices (the encapsulated cells were measured in air under the illumination of AM 1.5 G, 100 mW cm^{-2}. The temperature was 45~55 °C). (d) Extrapolated lifetime plot for the NDI-M-, NDI-S-, and NDI-B-based OSCs. The T80 values are extracted based on the function $y = ax + b$. (e) Results of PCEs and T80 lifetimes of the OSCs from previous studies and in this work.

q and $2 kT/q$. As shown in Figure S11, the OSCs with NDI-S, NDI-M, and ZnO exhibit the slopes of 1.12, 1.18, and 1.28 kT/q, respectively. It is obvious that the slopes of the devices with NDI-S and NDI-M are closer to kT/q, which indicates the suppression of the trap-assisted recombination in the devices. Transient photovoltage measurements were employed simultaneously and are shown in Figure S12. The carrier lifetimes (τ) are calculated to be 2.20, 1.63, and 1.09 μs for NDI-S, NDI-M, and ZnO devices, respectively. Thus, compared to the ZnO device, NDI-S and NDI-M devices restrained the trap-assisted recombination and induced an enhancement of the electron extraction to the cathode. These results demonstrate that NDI-S and NDI-M have electron extraction and transport capacities superior to ZnO, which explains the increased J_{SC} and FF of the NDI-S and NDI-M devices.

In addition to the enhancement in the device performance, the use of NDI-S and NDI-M molecules significantly improved the long-term stability of the inverted solar cells. In our previous work,[35] we have demonstrated that the ZnO CIL suffers from photo-instability due to its intrinsic ultraviolet (UV)-response that could result in poor stability of the OSCs, while the NDI-based CIL shows perfect and comprehensive stability. Therefore, in this work, our study of stability mainly focuses on the comparison of NDI-S, NDI-M, and NDI-B. First, the intrinsic stability of OSCs modified with these CILs was investigated. The devices with NDI-S, NDI-M, and NDI-B were encapsulated and kept in air ambient at room temperature. As shown in Figure 5a, OSCs modified with all these CILs could maintain over 95% of the initial PCE value after a storage time of 1464 h. These results suggest that the

use of NDI-S and NDI-M as CILs provides the benefits of good storage stability, which is the same as the use of NDI-B. Although the encapsulation can improve the storage stability of OSCs, the erosion problem of moisture ingression may occur through tiny crevices in the package during long-term operation. To evaluate the intrinsic resistance of OSCs to moisture, the stability of NDI-S-, NDI-M-, and NDI-B-based unencapsulated OSCs was investigated in an 80% RH environment at 25 °C. As shown in Figure 5b, the NDI-S-based cell shows the best intrinsic stability with the PCE keeping 93% of its initial value after a 168 h storage period. In contrast, the PCEs of the reference devices with NDI-M and NDI-B CILs degraded to 56 and 79% of their initial values, respectively. The normalized J_{SC}, FF, and V_{OC} of the OSCs under the exposure of 80% RH are depicted in Figure S13 as a function of exposure time. For the NDI-M device, the J_{SC}, FF, and V_{OC} exhibited obvious declines after being exposed to high RH for 160 h. While using the NDI-B CIL, the V_{OC} of the device was reduced to 80% of the initial value, indicating a deterioration of the electron collection ability. Notably, all the photovoltaic parameters of the NDI-S device could remain constant under the same conditions, suggesting that the NDI-S CIL can protect the device from moisture ingress to maintain the efficient electron extraction and transport properties. The device degradation in a humid atmosphere is commonly associated with the stability of active layer and interfacial contacts. Thus, the stability of the active layer under high R.H. conditions was first investigated by measuring the absorption spectra of the PBDB-TF:BTP-eC9 blend film. As shown in Figure S14, the absorption spectrum of PBDB-TF:BTP-eC9

remained unchanged after being stored under an 80% RH environment for 168 h, indicating that the high RH did not cause the decomposition of the active layer materials. Since the possible mechanism of device instability related to the decomposition of the active layer can be excluded, the discrepancy in intrinsic stability should lie in the CIL/active layer interfacial contact. The intrinsic stability of NDI-M and NDI-S was evaluated. The surface morphology and WF of CIL films after the aging process by saturated moisture vapor were characterized. Since the NDI-M film is readily destroyed through deliquescence in the high humidity environment, the intrinsic stability of NDI-M to moisture can hardly be characterized. The influence of high humidity on surface morphology and WF of NDI-B and NDI-S films was studied. The AFM results indicated that, after the storage of 168 h at 80% RH, the NDI-B and NDI-S films could retain smooth surfaces without observing any increase of R_q value (Figure S15a,b). The results indicate that the NDI-B and NDI-S films possess good chemical and morphological stability by resisting the erosion of moisture. Figure S16a,b presents the WF variations of the NDI-B and NDI-S films in an 80% RH environment. The WF of NDI-B showed an increase of approximately 0.11 eV after being stored for 168 h, while the WF of NDI-S remained almost unchanged under the same conditions. The unvaried WF value indicates that the good moisture resistance of NDI-S can maintain an efficient electron collection ability of the CIL, contributing to the high stability of the NDI-S-based OSCs. These results indicated that the degradation of device performance by moisture would be significantly affected by the difference in polar groups of CIL molecules. Compared with NDI-M and NDI-B, the extremely low hygroscopicity of NDI-S and the transition to a crystalline state under a high humidity environment enable NDI-S devices to exhibit excellent moisture resistance. Since OSCs are practically operated under irradiation for a long period, the long-term photostability of OSCs also should be concerned. The long-term photostability of the encapsulated NDI-S-, NDI-M-, and NDI-B-based OSCs was investigated in ambient air under continuous AM 1.5G illumination. As shown in Figure 5c, the NDI-S-, NDI-M-, or NDI-B-modified OSCs retained over 95% of the initial efficiency after 2100 h of continuous illumination. NDI-S and NDI-M are NDI-based molecules, which can effectively prevent organic photovoltaic materials from ultraviolet damage by converting the absorbed ultraviolet into photocurrent. The effect of NDI-based molecules on stability improvement of OSCs has been proved in our previous work.[35] Since the corrosion effect of ambient conditions and the long-term permeation of moisture can inevitably cause the degradation of OSC performances, we extrapolate the T80 lifetime (the time required to reach 80% of the initial PCE) of the solar cells according to the linear fitting of the photoaging period ranging from 0 to 2100 h (Figure 5d). The extrapolated T80 lifetimes of devices were found to be 28 228 h for NDI-S, 8378 h for NDI-M, and 16 456 h for NDI-B. This result confirms that the decreased hygroscopicity of NDI-S plays an essential role in improving the stability of OSCs. As summarized in Figure 5e,[52−56] to the best of our knowledge, the T80 lifetime value of NDI-S OSCs was among the best values for the OSCs ever reported, which will pave the way for the commercialization of OSC technology.

In summary, two naphthalene diimide derivatives NDI-M and NDI-S were synthesized to be utilized as CILs for inverted OSC devices. Compared with ZnO, the NDI-M and NDI-S

devices have the optimal PCE of about 17.3% based on PBDB-TF:BTP-eC9, which is among the highest photovoltaic efficiencies ever recorded in inverted OSC devices. This outstanding PCE could result from the better interfacial contact, improved charge carrier transportation, facilitated exciton dissociation, and depressed charge carrier recombination. The exceptional stability of the NDI-S device is further demonstrated by a T80 of over 28 000 h under operational conditions, which represents the best stability in the field of OSCs at present. Most importantly, the device modified with NDI-S exhibits excellent stability in an 80% RH environment. By using the DVS method, we demonstrate for the first time that the linkage of the counter ions with the host molecular structure in the zwitterion by the covalent bond can significantly reduce the hygroscopicity of the interlayer molecular, and the transformation of NDI-S from amorphous to crystalline trihydrate under a high RH environment can promote the reduction of moisture uptake, which further improves the stability of the device. Overall, the stability of NDI-S under a high humidity environment can significantly reduce the burden of device encapsulation, thus paving the way for the practical application of high-efficiency OSCs.

■ ASSOCIATED CONTENT

Ⓢ Supporting Information

The Supporting Information is available free of charge at https://pubs.acs.org/doi/10.1021/jacsau.2c00307.

> Experimental details, chemical structures of NDI-B, temporal adsorption profiles, PXRD spectra, I−V curve of the device, relationship between film thickness and UV−vis adsorption, dependence of device on the thickness of interfacial layer, J−V characteristics, energy level diagram, J−V curves of devices, Mott−Schottky analysis, light intensity dependence, charge carrier lifetime of solar cells, normalized J_{SC}, FF, and V_{OC}, optical absorption spectra, surface morphology and WF variations of films, and H NMR and ESI-MS spectra (PDF)

■ AUTHOR INFORMATION

Corresponding Authors

Bowei Xu − *State Key Laboratory of Chemical Resource Engineering, College of Materials Science and Engineering, Beijing University of Chemical Technology, Beijing 100029, China*; Email: xubowei@buct.edu.cn

Jianhui Hou − *State Key Laboratory of Polymer Physics and Chemistry, Beijing National Laboratory for Molecular Sciences, Institute of Chemistry, Chinese Academy of Sciences, Beijing 100190, P. R. China; University of Chinese Academy of Sciences, Beijing 100049, P. R. China*; ⓞ orcid.org/0000-0002-2105-6922; Email: hjhzlz@iccas.ac.cn

Authors

Qing Liao − *State Key Laboratory of Polymer Physics and Chemistry, Beijing National Laboratory for Molecular Sciences, Institute of Chemistry, Chinese Academy of Sciences, Beijing 100190, P. R. China; University of Chinese Academy of Sciences, Beijing 100049, P. R. China*

Qian Kang − *State Key Laboratory of Polymer Physics and Chemistry, Beijing National Laboratory for Molecular Sciences, Institute of Chemistry, Chinese Academy of Sciences,*

Beijing 100190, P. R. China; University of Chinese Academy of Sciences, Beijing 100049, P. R. China

Complete contact information is available at:
https://pubs.acs.org/10.1021/jacsau.2c00307

Notes

The authors declare no competing financial interest.

■ REFERENCES

(1) Krebs, F. C.; Espinosa, N.; Hösel, M.; Søndergaard, R. R.; Jørgensen, M. 25th Anniversary Article: Rise to Power - OPV-Based Solar Parks. *Adv. Mater.* **2014**, *26*, 29−39.

(2) Lu, L.; Zheng, T.; Wu, Q.; Schneider, A. M.; Zhao, D.; Yu, L. Recent Advances in Bulk Heterojunction Polymer Solar Cells. *Chem. Rev.* **2015**, *115*, 12666−12731.

(3) Zhao, W.; Zhang, S.; Zhang, Y.; Li, S.; Liu, X.; He, C.; Zheng, Z.; Hou, J. Environmentally Friendly Solvent-Processed Organic Solar Cells that are Highly Efficient and Adaptable for the Blade-Coating Method. *Adv. Mater.* **2018**, *30*, 1704837.

(4) Liu, C.; Xiao, C.; Xie, C.; Li, W. Flexible Organic Solar Cells: Materials, Large-area Fabrication Techniques and Potential Applications. *Nano Energy* **2021**, *89*, 106399.

(5) Dong, X.; Jiang, Y.; Sun, L.; Qin, F.; Zhou, X.; Lu, X.; Wang, W.; Zhou, Y. Large-Area Organic Solar Modules with Efficiency Over 14%. *Adv. Funct. Mater.* **2022**, *32*, 2110209.

(6) Cui, Y.; Xu, Y.; Yao, H.; Bi, P.; Hong, L.; Zhang, J.; Zu, Y.; Zhang, T.; Qin, J.; Ren, J.; Chen, Z.; He, C.; Hao, X.; Wei, Z.; Hou, J. Single-Junction Organic Photovoltaic Cell with 19% Efficiency. *Adv. Mater.* **2021**, *33*, 2102420.

(7) Liu, L.; Chen, S.; Qu, Y.; Gao, X.; Han, L.; Lin, Z.; Yang, L.; Wang, W.; Zheng, N.; Liang, Y.; Tan, Y.; Xia, H.; He, F. Nanographene-Osmapentalyne Complexes as a Cathode Interlayer in Organic Solar Cells Enhance Efficiency over 18%. *Adv. Mater.* **2021**, *33*, 2101279.

(8) Cui, Y.; Yao, H.; Zhang, J.; Xian, K.; Zhang, T.; Hong, L.; Wang, Y.; Xu, Y.; Ma, K.; An, C.; He, C.; Wei, Z.; Gao, F.; Hou, J. Single-Junction Organic Photovoltaic Cells with Approaching 18% Efficiency. *Adv. Mater.* **2020**, *32*, No. e1908205.

(9) Xu, X.; Yu, L.; Meng, H.; Dai, L.; Yan, H.; Li, R.; Peng, Q. Polymer Solar Cells with 18.74% Efficiency: From Bulk Heterojunction to Interdigitated Bulk Heterojunction. *Adv. Funct. Mater.* **2022**, *32*, 2108797.

(10) Yu, K.; Song, W.; Li, Y.; Chen, Z.; Ge, J.; Yang, D.; Zhang, J.; Xie, L.; Liu, C.; Ge, Z. Achieving 18.14% Efficiency of Ternary Organic Solar Cells with Alloyed Nonfullerene Acceptor. *Small Struct.* **2021**, *2*, 2100099.

(11) Meng, H.; Liao, C.; Deng, M.; Xu, X.; Yu, L.; Peng, Q. 18.77 % Efficiency Organic Solar Cells Promoted by Aqueous Solution Processed Cobalt (II) Acetate Hole Transporting Layer. *Angew. Chem., Int. Ed.* **2021**, *60*, 22554−22561.

(12) Xu, X.; Li, D.; Yuan, J.; Zhou, Y.; Zou, Y. Recent Advances in Stability of Organic Solar Cells. *EnergyChem* **2021**, *3*, 100046.

(13) Park, S.; Kim, T.; Yoon, S.; Koh, C. W.; Woo, H. Y.; Son, H. J. Progress in Materials, Solution Processes, and Long-Term Stability for Large-Area Organic Photovoltaics. *Adv. Mater.* **2020**, *32*, 2002217.

(14) Duan, L.; Uddin, A. Progress in Stability of Organic Solar Cells. *Adv. Sci.* **2020**, *7*, 1903259.

(15) Zhang, K.; Xia, R.; Fan, B.; Liu, X.; Wang, Z.; Dong, S.; Yip, H. L.; Ying, L.; Huang, F.; Cao, Y. 11.2% All-Polymer Tandem Solar Cells with Simultaneously Improved Efficiency and Stability. *Adv. Mater.* **2018**, *30*, 1803166.

(16) Song, J.; Tyagi, P.; An, K.; Park, M.; Jung, H.; Ahn, N.; Choi, M.; Lee, D.; Lee, C. Degradation of Electrical Characteristics in Low-bandgap Polymer Solar Cells Associated with Light-induced Aging. *Org. Electron.* **2020**, *81*, 105686.

(17) Weng, C.-N.; Yang, H.-C.; Tsai, C.-Y.; Chen, S.-H.; Chen, Y.-S.; Chen, C.-H.; Huang, K.-M.; Meng, H.-F.; Chao, Y.-C.; Chang, C.-Y.; Zan, H.-W.; Horng, S.-F.; Yu, P.-C.; Su, K.-W. The Influence of UV Filter and Al/Ag Moisture Barrier Layer on the Outdoor Stability of Polymer Solar Cells. *Sol. Energy* **2020**, *199*, 308−316.

(18) Jiang, Y.; Sun, L.; Jiang, F.; Xie, C.; Hu, L.; Dong, X.; Qin, F.; Liu, T.; Hu, L.; Jiang, X.; Zhou, Y. Photocatalytic effect of ZnO on the stability of nonfullerene acceptors and its mitigation by SnO2 for nonfullerene organic solar cells. *Mater. Horiz.* **2019**, *6*, 1438−1443.

(19) Classen, A.; Heumueller, T.; Wabra, I.; Gerner, J.; He, Y.; Einsiedler, L.; Li, N.; Matt, G. J.; Osvet, A.; Du, X.; Hirsch, A.; Brabec, C. J. Revealing Hidden UV Instabilities in Organic Solar Cells by Correlating Device and Material Stability. *Adv. Energy Mater.* **2019**, *9*, 1902124.

(20) Zhu, Q.; Xue, J.; Zhang, L.; Wen, J.; Lin, B.; Naveed, H. B.; Bi, Z.; Xin, J.; Zhao, H.; Zhao, C.; Zhou, K.; Liu, S.; Ma, W. Intermolecular Interaction Control Enables Co-optimization of Efficiency, Deformability, Mechanical and Thermal Stability of Stretchable Organic Solar Cells. *Small* **2021**, *17*, 2007011.

(21) Hung, K. E.; Lin, Y. S.; Xue, Y. J.; Yang, H. R.; Lai, Y. Y.; Chang, J. W.; Su, C. J.; Su, A. C.; Hsu, C. S.; Jeng, U. S.; Cheng, Y. J. Non-Volatile Perfluorophenyl-Based Additive for Enhanced Efficiency and Thermal Stability of Nonfullerene Organic Solar Cells via Supramolecular Fluorinated Interactions. *Adv. Energy Mater.* **2022**, *12*, 2103702.

(22) Duan, T.; Wu, Y.; Yang, K.; Oh, J.; Yang, C.; Chen, S.; Zhong, C.; Yu, D.; Zhao, Y.; Lu, S. Significantly Enhanced Thermal Stability from a New Kind of N-type Organic Semiconductor DFA4: A Fully Fused F8IC. *J. Mater. Chem. C* **2021**, *9*, 13625−13629.

(23) Soultati, A.; Fakharuddin, A.; Polydorou, E.; Drivas, C.; Kaltzoglou, A.; Haider, M. I.; Kournoutas, F.; Fakis, M.; Palilis, L. C.; Kennou, S.; Davazoglou, D.; Falaras, P.; Argitis, P.; Gardelis, S.; Kordatos, A.; Chroneos, A.; Schmidt-Mende, L.; Vasilopoulou, M. Lithium Doping of ZnO for High Efficiency and Stability Fullerene and Non-fullerene Organic Solar Cells. *ACS Appl. Energy Mater.* **2019**, *2*, 1663−1675.

(24) Sadeghianlemraski, M.; Lee, B. Y.; Davidson-Hall, T.; Leonenko, Z.; Aziz, H. Enhanced Photo-stability of Inverted Organic Solar cells via Using Polyethylenimine in the Electron Extraction Layers. *Org. Electron.* **2019**, *73*, 26−35.

(25) Burlingame, Q.; Ball, M.; Loo, Y.-L. It's time to focus on organic solar cell stability. *Nat. Energy* **2020**, *5*, 947−949.

(26) Norrman, K.; Gevorgyan, S. A.; Krebs, F. C. Water-Induced Degradation of Polymer Solar Cells Studied by H218O Labeling. *ACS Appl. Mater. Interfaces* **2009**, *1*, 102−112.

(27) Klumbies, H.; Karl, M.; Hermenau, M.; Rösch, R.; Seeland, M.; Hoppe, H.; Müller-Meskamp, L.; Leo, K. Water Ingress Into and Climate Dependent Lifetime of Organic Photovoltaic Cells Investigated by Calcium Corrosion Tests. *Sol. Energy Mater. Sol. Cells* **2014**, *120*, 685−690.

(28) Züfle, S.; Neukom, M. T.; Altazin, S.; Zinggeler, M.; Chrapa, M.; Offermans, T.; Ruhstaller, B. An Effective Area Approach to Model Lateral Degradation in Organic Solar Cells. *Adv. Energy Mater.* **2015**, *5*, 1500835.

(29) Norrman, K.; Madsen, M. V.; Gevorgyan, S. A.; Krebs, F. C. Degradation Patterns in Water and Oxygen of an Inverted Polymer Solar Cell. *J. Am. Chem. Soc.* **2010**, *132*, 16883−16892.

(30) Sapkota, S. B.; Spies, A.; Zimmermann, B.; Dürr, I.; Würfel, U. Promising Long-term Stability of Encapsulated ITO-free Bulk-heterojunction Organic Solar Cells under Different Aging Conditions. *Sol. Energy Mater. Sol. Cells* **2014**, *130*, 144−150.

(31) Yamaguchi, H.; Granstrom, J.; Nie, W.; Sojoudi, H.; Fujita, T.; Voiry, D.; Chen, M.; Gupta, G.; Mohite, A. D.; Graham, S.;

Chhowalla, M. Reduced Graphene Oxide Thin Films as Ultrabarriers for Organic Electronics. *Adv. Energy Mater.* **2014**, *4*, 1300986.

(32) Kim, T.; Kang, J. H.; Yang, S. J.; Sung, S. J.; Kim, Y. S.; Park, C. R. Facile Preparation of Reduced Graphene Oxide-based Gas Barrier Films for Organic Photovoltaic Devices. *Energy Environ. Sci.* **2014**, *7*, 3403−3411.

(33) Chen, N.; Kovacik, P.; Howden, R. M.; Wang, X.; Lee, S.; Gleason, K. K. Low Substrate Temperature Encapsulation for Flexible Electrodes and Organic Photovoltaics. *Adv. Energy Mater.* **2015**, *5*, 1401442.

(34) Clark, M. D.; Maschmann, M. R.; Patel, R. J.; Leever, B. J. Scratch Resistance and Durability Enhancement of Bulk Heterojunction Organic Photovoltaics Using Ultra-thin Alumina Layers. *Sol. Energy Mater. Sol. Cells* **2014**, *128*, 178−183.

(35) Liao, Q.; Kang, Q.; Yang, Y.; Zheng, Z.; Qin, J.; Xu, B.; Hou, J. Highly Stable Organic Solar Cells Based on an Ultraviolet-Resistant Cathode Interfacial Layer. *CCS Chem.* **2022**, *4*, 1059−1069.

(36) Shao, S.; Liu, J.; Bergqvist, J.; Shi, S.; Veit, C.; Würfel, U.; Xie, Z.; Zhang, F. In Situ Formation of MoO3in PEDOT:PSS Matrix: A Facile Way to Produce a Smooth and Less Hygroscopic Hole Transport Layer for Highly Stable Polymer Bulk Heterojunction Solar Cells. *Adv. Energy Mater.* **2013**, *3*, 349−355.

(37) Vohra, V.; Kawashima, K.; Kakara, T.; Koganezawa, T.; Osaka, I.; Takimiya, K.; Murata, H. Efficient Inverted Polymer Solar Cells Employing Favourable Molecular Orientation. *Nat. Photonics* **2015**, *9*, 403−408.

(38) Salameh, A. K.; Mauer, L. J.; Taylor, L. S. Deliquescence Lowering in Food Ingredient Mixtures. *J. Food Sci.* **2006**, *71*, E10−E16.

(39) Allan, M.; Mauer, L. J. Comparison of Methods for Determining the Deliquescence Points of Single Crystalline Ingredients and Blends. *Food Chem.* **2016**, *195*, 29−38.

(40) Tian, F.; Qu, H.; Zimmermann, A.; Munk, T.; Jørgensen, A. C.; Rantanen, J. Factors Affecting Crystallization of Hydrates. *J. Pharm. Pharmacol.* **2010**, *62*, 1534−1546.

(41) Cui, Y.; Yao, E. Evaluation of Hydrate-screening Methods. *J. Pharm. Sci.* **2008**, *97*, 2730−2744.

(42) Hancock, B. C.; Shamblin, S. L. Water Vapour Sorption by Pharmaceutical Sugars. *Pharm. Sci. Technol. Today* **1998**, *1*, 345−351.

(43) Buckton, G. Characterisation of Small Changes in the Physical Properties of Powders of Significance for Dry Powder Inhaler Formulations. *Adv. Drug Delivery Rev.* **1997**, *26*, 17−27.

(44) Chen, Q.; Wang, C.; Li, Y.; Chen, L. Interfacial Dipole in Organic and Perovskite Solar Cells. *J. Am. Chem. Soc.* **2020**, *142*, 18281−18292.

(45) Cheng, P.; Li, G.; Zhan, X.; Yang, Y. Next-generation Organic Photovoltaics Based on Non-fullerene Acceptors. *Nat. Photonics* **2018**, *12*, 131−142.

(46) Zhou, H.; Zhang, Y.; Seifter, J.; Collins, S. D.; Luo, C.; Bazan, G. C.; Nguyen, T. Q.; Heeger, A. J. High-Efficiency Polymer Solar Cells Enhanced by Solvent Treatment. *Adv. Mater.* **2013**, *25*, 1646−1652.

(47) Xu, H.; Zou, H.; Zhou, D.; Zeng, G.; Chen, L.; Liao, X.; Chen, Y. Printable Hole Transport Layer for 1.0 cm^2 Organic Solar Cells. *ACS Appl. Mater. Interfaces* **2020**, *12*, 52028−52037.

(48) Dong, S.; Zhang, K.; Liu, X.; Yin, Q.; Yip, H.-L.; Huang, F.; Cao, Y. Efficient Organic-inorganic Hybrid Cathode Interfacial Layer Enabled by Polymeric Dopant and its Application in Large-area Polymer Solar Cells. *Sci. China Chem.* **2018**, *62*, 67−73.

(49) Zhang, Y.; Liu, D.; Lau, T. K.; Zhan, L.; Shen, D.; Fong, P. W. K.; Yan, C.; Zhang, S.; Lu, X.; Lee, C. S.; Hou, J.; Chen, H.; Li, G. A Novel Wide-Bandgap Polymer with Deep Ionization Potential Enables Exceeding 16% Efficiency in Ternary Nonfullerene Polymer Solar Cells. *Adv. Funct. Mater.* **2020**, *30*, 1910466.

(50) Cowan, S. R.; Roy, A.; Heeger, A. J. Recombination in Polymer-fullerene Bulk Heterojunction Solar Cells. *Phys. Rev. B* **2010**, *82*, 245207.

(51) Kyaw, A. K.; Wang, D. H.; Gupta, V.; Leong, W. L.; Ke, L.; Bazan, G. C.; Heeger, A. J. Intensity Dependence of Current-voltage Characteristics and Recombination in High-efficiency Solution-processed Small-molecule Solar Cells. *ACS Nano* **2013**, *7*, 4569−4577.

(52) Han, Y.; Dong, H.; Pan, W.; Liu, B.; Chen, X.; Huang, R.; Li, Z.; Li, F.; Luo, Q.; Zhang, J.; Wei, Z.; Ma, C. Q. An Efficiency of 16.46% and a T80 Lifetime of Over 4000 h for the PM6:Y6 Inverted Organic Solar Cells Enabled by Surface Acid Treatment of the Zinc Oxide Electron Transporting Layer. *ACS Appl. Mater. Interfaces* **2021**, *13*, 17869−17881.

(53) Du, X.; Heumueller, T.; Gruber, W.; Classen, A.; Unruh, T.; Li, N.; Brabec, C. J. Efficient Polymer Solar Cells Based on Non-fullerene Acceptors with Potential Device Lifetime Approaching 10 Years. *Joule* **2019**, *3*, 215−226.

(54) Gasparini, N.; Salvador, M.; Strohm, S.; Heumueller, T.; Levchuk, I.; Wadsworth, A.; Bannock, J. H.; de Mello, J. C.; Baran, H.-J.; McCulloch, D.; Brabec, I.; Brabec, C. J. Burn-in Free Nonfullerene-Based Organic Solar Cells. *Adv. Energy Mater.* **2017**, *7*, 1700770.

(55) Xiao, J.; Ren, M.; Zhang, G.; Wang, J.; Zhang, D.; Liu, L.; Li, N.; Brabec, C. J.; Yip, H.-L.; Cao, Y. An Operando Study on the Photostability of Nonfullerene Organic Solar Cells. *Sol. RRL* **2019**, *3*, 1900077.

(56) Xu, X.; Xiao, J.; Zhang, G.; Wei, L.; Jiao, X.; Yip, H.-L.; Cao, Y. Interface-enhanced Organic Solar Cells with Extrapolated T80 Lifetimes of over 20 Years. *Sci. Bull.* **2020**, *65*, 208−216.